applied sciences

MDPI

Article

Optimization of the Measurement Technique for Emissions in Reverberation Chamber Using the Equivalence Principle

Alfredo De Leo *, Graziano Cerri, Paola Russo and Valter Mariani Primiani

Department of Information Engineering, Università Politecnica delle Marche, 60131 Ancona, Italy; g.cerri@univpm.it (G.C.); paola.russo@univpm.it (P.R.); v.mariani@univpm.it (V.M.P.)
* Correspondence: a.deleo@univpm.it

Abstract: This paper presents an optimization of a method to reconstruct the radiated emissions of an equipment under test by the measurement of the electric field samples collected on the walls of a reverberation chamber. This means that only the orthogonal component of the electric field is necessary to obtain the radiative behavior of the device in free space conditions. The use of the equivalence principle allows one to reduce the number of equivalent sources used to reconstruct the radiation of the device. In fact, in the previous version of the method, the sources are placed into the entirety of working volume of the reverberation chamber. In the current version of the method, only the surface surrounding the equipment under test is discretized. The analytical implementation of the method is proposed for a particular stirring action: the multiple monopole source stirring technique. This technique is based on an array of monopoles placed onto the walls of the cavity, and therefore no further hardware is needed for the reconstruction of the radiated emissions. The method is experimentally validated in a real scenario.

Keywords: reverberation chamber; radiated emissions; electromagnetic compatibility; equivalent sources

Citation: De Leo, A.; Cerri, G.; Russo, P.; Mariani Primiani, V. Optimization of the Measurement Technique for Emissions in Reverberation Chamber Using the Equivalence Principle. *Appl. Sci.* **2021**, *11*, 7696. https://doi.org/10.3390/app11167696

Academic Editor: Adel Razek

Received: 22 July 2021
Accepted: 20 August 2021
Published: 21 August 2021

1. Introduction

The measurement of radiated emissions is a fundamental aspect in electromagnetic compatibility; in fact, in order to ensure the correct behavior of several devices in the same environment, it is necessary to establish maximum emission and minimum immunity limits.

Historically, the first measurement environment was the open-air test site (OATS), which was subsequently substituted by anechoic alternative test sites as anechoic chambers and TEM or GTEM cells. For this reason, how to correlate the measurements performed in these sites to OATS conditions has been investigated. In this direction, [1–7] introduced a set of equivalent sources to replace the equipment under test (EUT) and to extrapolate the radiation in free space conditions from the measurements performed in these alternative sites.

Nowadays, one of the alternative sites that has been more extensively investigated in electromagnetic compatibility research is the reverberation chamber (RC). An RC is a metallic enclosure where the electromagnetic field is properly stirred to be statistically uniform, unpolarized, and anisotropic. There are two main typologies of stirring actions: mechanical stirring and source stirring. The first is based on the variation of the boundary conditions by rotating metallic paddles [8], or by moving [9] or vibrating [10] the RC's walls. The second kind of stirring technique acts on the source [11] by varying its positions or its frequency and therefore its coupling with the eigenmodes of the chamber. In this second set of actions, the multiple monopole source stirring (MMSS) technique was developed [12], validated [13], and successfully compared to the other techniques [14,15].

The standard rules [16] support the use of RCs as an alternative site for EMC measurements. In particular, for the radiation emission measurements, the value of the maximum

electric field radiated by the EUT is derived from the measurement of its average total radiated power and the estimation of the directivity of the EUT, analytically derived by its geometrical dimensions.

Recently, a novel method was proposed [17] to directly reconstruct the emissions of an EUT by an RC. It is based on the measurement of a set of samples of electric fields collected on the walls of the RC, and subsequently on the setting of equivalent sources able to provide the emission values in free space conditions. The main advantage of this method is that the value of the electric field over all the directions is directly obtained, avoiding the estimation of the directivity of the EUT, without moving or rotating neither antennas nor EUT.

In the generalized formulation of the method, six equivalent sources are placed at each point of a volumetric grid, placed in the whole volume containing the EUT. The main scope of this paper is to improve the method's computational efficiency through the reduction of the number of equivalent sources, obtained by enforcing the equivalence principle.

In fact, the equivalence principle states that the radiation of a device can be described in terms of the only electric and magnetic currents tangential to a closed surface surrounding the device. According to this formulation, only four equivalent current components are necessary for each point of the equivalence surface. Therefore, by passing from a 3D to a 2D distribution of the equivalent sources, the problem complexity is strongly reduced without losing accuracy.

The traditional application of the equivalence principle is based on a direct measurement of the tangential electric and magnetic field components on the equivalence surface. In our case, the EUT is inside an RC where the antennas are located on its walls, so we extrapolate the complex value of the equivalent currents by measuring only the electric field component normal to the RC walls.

Under the assumption that the power radiated by a device inside an RC and the one radiated in free space are the same, the estimation of the EUT emission can be carried out in three steps. In the first step, the EUT is placed in the working volume of the RC and the radiated field is measured in a number of selected points on the RC walls. In the second step, from the knowledge of these field samples, the values of the equivalent sources that characterize the EUT radiation are evaluated. In the third step, the equivalent currents are considered to be radiating in free space, and the emission of the EUT is finally evaluated.

In this paper, we focus our investigation on step two, concerning the evaluation of the equivalent sources. In particular, the aim of this paper is to improve the efficiency of the method, reducing the number of equivalent sources used to reconstruct the emission of the EUT. In fact, in the previous version of the method, six equivalent sources (three electric and three magnetic dipoles) were needed in each grid point, and the grid points were regularly placed in the whole volume containing the EUT. In the current formulation of the method, the surface including the EUT is discretized into sub surfaces, and in each of them four equivalent sources (magnetic and electric current densities) are considered.

The paper is organized as follows: Section 2 describes the scenario of an RC where the MMSS technique is implemented, the method, and the analytical formulation, using the equivalence principle; Section 3 reports the experimental results obtained, applying the proposed method in a real scenario, and their comparison with numerical simulations and more traditional anechoic environment measurements. Finally, discussion on the results and conclusions are reported in Sections 4 and 5, respectively.

2. Formulation of the Problem

The reference scenario is a reverberation chamber made by a rectangular cavity having dimensions a along x direction, b along y direction, and c along z direction, as shown in Figure 1. The walls of the chamber have a finite conductivity that accounts for all the loss mechanisms, and its value is chosen to have the same quality factor obtained by measurements [13]. A set of N_S monopoles is placed on the RC's walls to achieve the field sampling. The EUT is placed into the working volume of the RC.

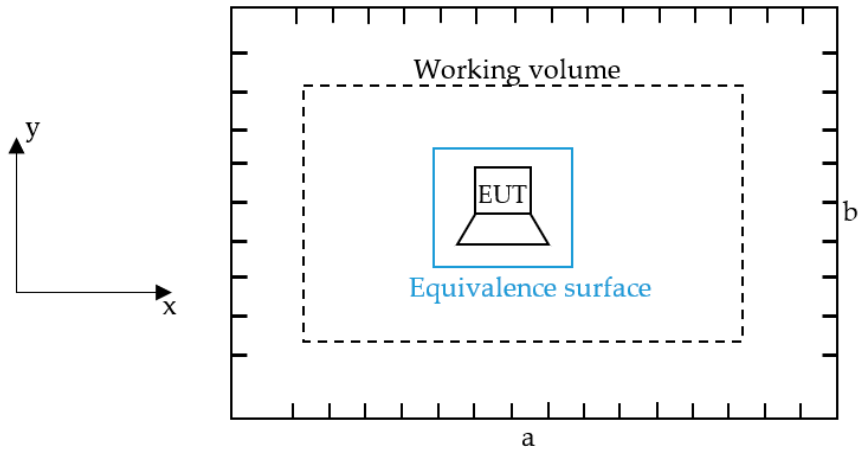

Figure 1. The scenario: an RC, its dimensions, the working volume, and the equivalence surface surrounding the EUT.

The application of the equivalence theorem involves the use of a closed geometrical surface (equivalence surface) surrounding the radiating object. In our case, it is a rectangular surface whose faces are parallel to the RC's walls, and it is the geometrical support where the electric ($\vec{J_{eq}}$) and magnetic ($\vec{M_{eq}}$) equivalent currents, which characterize the EUT radiation, flow. No particular constraint limits the choice of the equivalent surface, whose shape is due to practical reasons.

The equivalent current distribution is discretized by introducing a proper discretization of the equivalence surface: each face is divided into a set of small rectangular sub-areas. If each sub-area is small enough, with respect to the wavelength, the current distribution on each sub-area can be considered constant.

For example, Figure 2 shows a rectangular face of the equivalence surface orthogonal to the x axis, and the i-th sub-area (S) having dimensions $(2\Delta_y, 2\Delta_z)$, centered in (x_H, y_H, z_H).

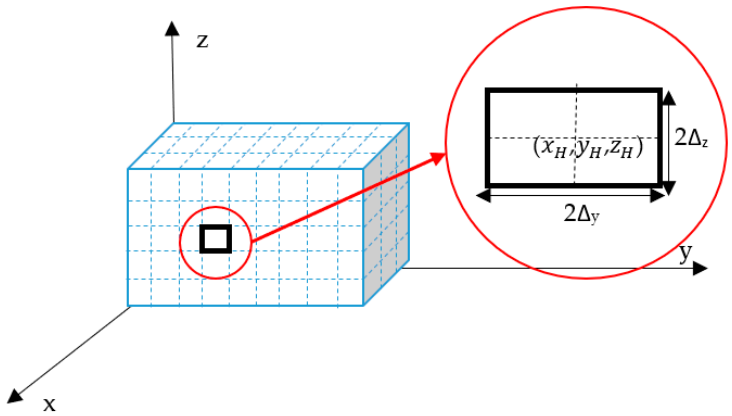

Figure 2. Sub-surface element in the face orthogonal to x axis and its coordinates and dimensions.

In this case, the equivalent magnetic and electric currents are Equation (1)

$$\begin{cases} \overline{M_{eq}^i} = M_{eqy}^i \hat{y} + M_{eqz}^i \hat{z} \\ \overline{J_{eq}^i} = J_{eqy}^i \hat{y} + J_{eqz}^i \hat{z} \end{cases} \qquad i = 1, \ldots, N_{eq}^{(x)} \tag{1}$$

where $N_{eq}^{(x)}$ is the total number of sub-areas after the discretization of the considered face.

Equation (1) clearly shows that, for each sub-area, four current components must be determined to characterize the EUT emission. Similar expressions can be easily obtained for the other faces.

The electric field radiated by the equivalent currents in a rectangular cavity can be calculated using a modal expansion [18], including irrotational and TE and TM solenoidal fields (2).

$$\overline{E} = \overline{E}_{IRR} + \overline{E}_{TE} + \overline{E}_{TM} \tag{2}$$

The irrotational component of the electric field is (3)

$$\overline{E}_{IRR} = -\frac{1}{j\omega\varepsilon} \sum_{m,n,p} \left(\int_S \overline{J}_{eq} \cdot \overline{f}_{m,n,p} dS \right) \overline{f}_{m,n,p} \tag{3}$$

and the solenoidal components are (4):

$$\overline{E}_{TE,TM} = \sum_{m,n,p} \left[\frac{\int_S \overline{M}_{eq} \cdot \overline{h}^{TE,TM}_{m,n,p} dS - j\omega\mu \int_S \overline{J}_{eq} \cdot \overline{e}^{TE,TM}_{m,n,p} dS}{k^2_{m,n,p} - \beta^2_{TE,TM}} \right] \overline{e}^{TE,TM}_{m,n,p}, \tag{4}$$

where

$$\beta^2_{TE,TM} = \beta^2 \left[1 - (-1+j) \frac{\omega_{n,m,p}}{\omega Q^{TE,TM}_{m,n,p}} \right], \tag{5}$$

$\overline{f}_{m,n,p}$ and $\overline{e}^{TE,TM}_{m,n,p}$ are irrotational and TE and TM are divergenceless electric eigenvectors, respectively, whereas $\overline{h}^{TE,TM}_{m,n,p}$ are the TE and TM divergenceless magnetic eigenvectors.

$k_{m,n,p}$, $Q^{TE,TM}_{m,n,p}$, and $\omega_{n,m,p}$ are the corresponding eigenvalues, quality factors, and resonant angular frequencies, respectively, and $\beta^2 = \omega^2\mu\epsilon$. The $Q^{TE,TM}_{m,n,p}$ is the quality factor of each mode, and it is calculated considering an equivalent wall conductivity value retrieved from real chamber quality factor measurements [13,15], thus accounting for all loss mechanisms inside the real RC. The equivalent wall conductivity may change with the frequency, and it does not depend on the equivalent surface choice.

Because of discretization, applying the superposition of the effects, (2) can be written as:

$$\vec{E} = \sum_{i=1}^{N_{eq}} \left(\vec{E}^{i}_{IRR} + \vec{E}^{i}_{TE} + \vec{E}^{i}_{TM} \right), \tag{6}$$

where each term can be evaluated solving the integrals in (5) and (6). In particular, the electric field radiated by the equivalent currents of the i-th sub-area in a generic point $P(x,y,z)$ is expressed by (7), (8) and (9).

$$\begin{aligned} \overline{E^i}_{IRR}(x,y,z) = & -\frac{1}{j\omega\varepsilon} \frac{32}{abc} \sum_{m,n,p} \frac{1}{k^2_{m,n,p}} \sin(k_x x_H) \sin(k_y \Delta_y) \sin(k_z \Delta_z) \left[\frac{J^i_{eqz} \sin(k_y y_H) \cos(k_z z_H)}{k_y} \right. \\ & \left. + \frac{J^i_{eqy} \cos(k_y y_H) \sin(k_z z_H)}{k_z} \right] \begin{cases} k_x \cos(k_x x) \sin(k_y y) \sin(k_z z) \hat{x} \\ k_y \sin(k_x x) \cos(k_y y) \sin(k_z z) \hat{y} \\ k_z \sin(k_x x) \sin(k_y y) \cos(k_z z) \hat{z} \end{cases}, \end{aligned} \tag{7}$$

$$\begin{aligned} \overline{E^i}_{TE}(x,y,z) = & \frac{32}{abc\delta_m\delta_n} \sum_{m,n,p} \frac{1}{k^2_{m,n,p} - \beta^2_{TE}} \sin(k_y \Delta_y) \sin(k_z \Delta_z) \left\{ \cos(k_x x_H) \left[\frac{M^i_{eqy} \sin(k_y y_H) \cos(k_z z_H)}{k^2_c} \right. \right. \\ & \left. \left. - \frac{M^i_{eqz} \cos(k_y y_H) \sin(k_z z_H)}{k_y \, k_z} \right] - j\omega\mu \frac{k_x}{k^2_c k_y \, k_z} J^i_{eqy} \sin(k_x x_H) \cos(k_y y_H) \sin(k_z z_H) \right\} \\ & \begin{cases} -k_y \cos(k_x x) \sin(k_y y) \sin(k_z z) \hat{x} \\ k_x \sin(k_x x) \cos(k_y y) \sin(k_z z) \hat{y} \end{cases} \end{aligned} \tag{8}$$

$$\overline{E^i}_{TM}(x,y,z) = \frac{32}{a\ b\ c\ \delta_p} \sum_{m,n,p} \frac{1}{k^2_{m,n,p} - \beta^2_{TM}} \sin(k_y \Delta_y) \sin(k_z \Delta_z) \Big\{ M^i_{eqy} \cos(k_x x_H) \sin(k_y y_H) \cos(k_z z_H) - j\omega\mu \frac{k_c^2}{k^2_{m,n,p}} \sin(k_x x_H) \left[\frac{J^i_{eqz} \sin(k_y y_H) \cos(k_z z_H)}{k_y\ k_z} - \frac{J^i_{eqy} \cos(k_y y_H) \sin(k_z z_H)}{k_c^2} \right] \Big\} \begin{cases} k_x \cos(k_x x) \sin(k_y y) \sin(k_z z) \hat{x} \\ k_y \sin(k_x x) \cos(k_y y) \sin(k_z z) \hat{y} \\ k_z \sin(k_x x) \sin(k_y y) \cos(k_z z) \hat{z} \end{cases}, \quad (9)$$

where $\delta_k = \begin{cases} 1, & k \neq 0 \\ 2, & k = 0 \end{cases}$

and $k_x = \frac{m\pi}{a}, k_y = \frac{n\pi}{b}, k_x = \frac{p\pi}{c}$.

Similar expressions can be found for the faces oriented along the y and z directions. For a better readability of the manuscript, they are reported in the Appendix A.

The algorithm to reconstruct the radiated emission in free space of an EUT placed into an RC is detailed in [17] and here briefly reported in the flow chart of Figure 3, for the sake of completeness.

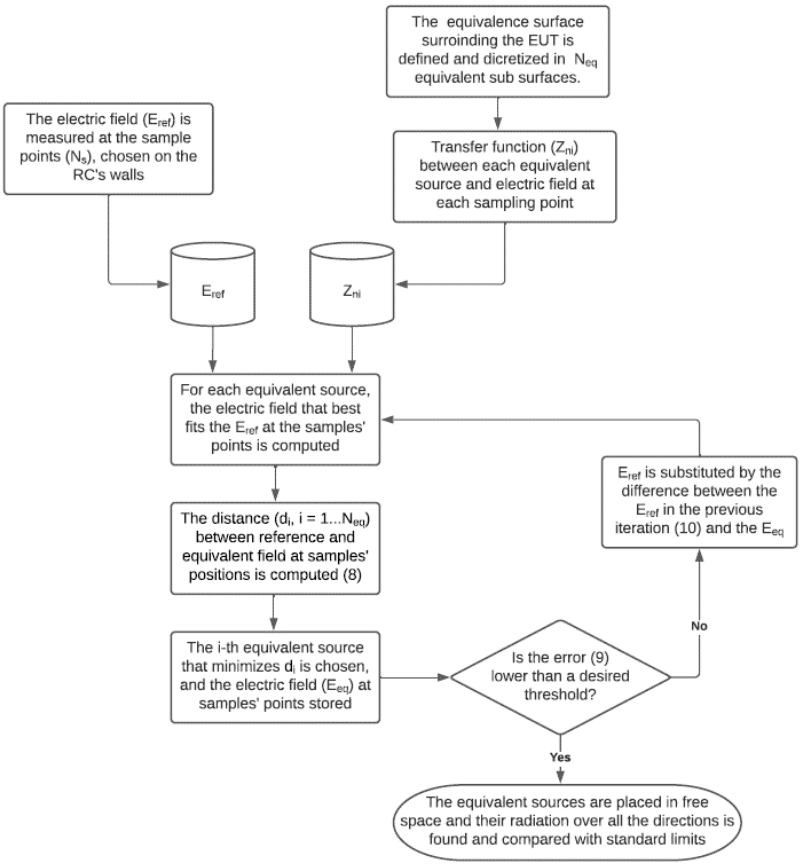

Figure 3. Flow chart of the algorithm for the reconstruction of the radiated emissions.

Two set of data are required. The first one is the value of the electric field measured at the samples' positions. The second one is the Z_{ni} matrix that represents the analytical transfer function between each equivalent source and the electric field at sample position.

Four equivalent sources are placed in each sub surface in which the whole equivalence surface is discretized.

At first, the algorithm evaluates the field due to each equivalent current in all sample positions. Then the distance between this field and the reference field is computed at the samples' positions according to (10):

$$d_i = \frac{\sum_{n=1}^{N_s} |E_n^{res} - Z_{ni} I_i|}{\sum_{n=1}^{Ns} |E_n^{res}|}, \quad i = 1, \ldots, N_{eq} \tag{10}$$

where I_i represents the i-th equivalent source (J_{eq}^i or M_{eq}^i) and each element of the matrix Z_{ni} represents the electric field generated by the i-th equivalent source and normalized to I_i, calculated at the n-th sample point.

Subsequently, the $i^* - th$ equivalent source, which minimizes d_i, is chosen and the residual electric field, computed at each iteration, is (11):

$$E_n^{res} = E_n^{res} - Z_{ni*} I_{i^*}, \; n = 1, \ldots, N_s \tag{11}$$

The relative error checked to decide when terminating the iteration is (12):

$$err = \frac{\sum_{n=1}^{N_s} |E_n^{res}|}{\sum_{n=1}^{N_s} \left| E_n^{ref} \right|}. \tag{12}$$

Iterations terminate when err is lower than a desired threshold.

3. Results

The model was applied to the EUT reported in Figure 4a. It is a metallic box having the dimensions 200 mm × 90 mm × 100 mm, with a rectangular slot (length 75 mm, height 5 mm), centered in the face 200 mm × 90 mm. The EUT is fed by a folded dipole connected to the central conductor of an SMA pass-through connector. The EUT was placed into the working volume of a rectangular RC, with the dimensions a = 800 mm, b = 900 mm, and c = 1000 mm.

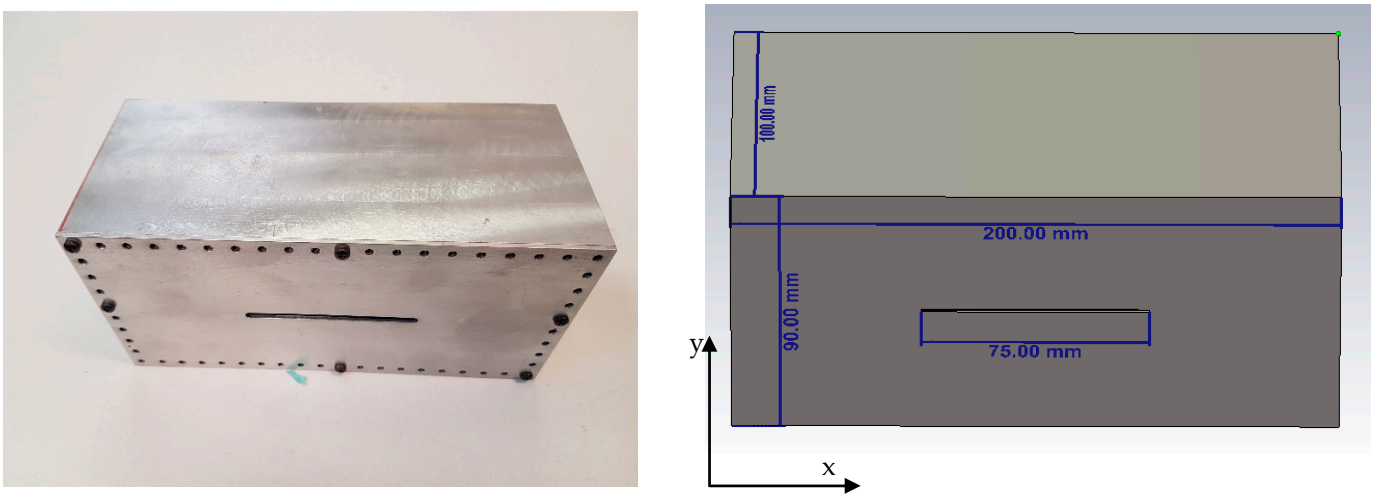

(**a**) (**b**)

Figure 4. The EUT: (**a**) The real device, used for emission measurements in the reverberation chamber and in the anechoic environment; (**b**) The numerical model, used for full wave simulations.

In order to verify the model, the radiation of the EUT was simulated using a full wave numerical tool (Figure 4b) and subsequently measured in an anechoic environment (AE).

As regards RC measurements, a vector network analyzer (VNA) was used to measure the scattering matrix between the port used to feed the EUT, and the port was sequentially connected to each monopole placed onto the walls of the RC. Therefore, the VNA measured the amplitude and phase of the parameters of all 2-port scattering matrices because the method, in the proposed formulation, is based on the knowledge of the complex value of the electric field collected at the samples' position.

The numerical tool used for simulation is the CST Microwave Studio; in particular, a frequency domain solver was used because we were interested in obtaining results at a single frequency (2 GHz).

Measurements in AE were performed by a VNA, used to feed the EUT, connected to port 1 of the instrument. The electric field was measured using a calibrated double ridge horn antenna, connected to port 2 of the VNA. The EUT is located on a turntable, and two planes were considered in these measurements: the E-plane ($\phi = 90^\circ$, varying θ) and the H-plane ($\phi = 0^\circ$, varying θ). During these measurements, the antenna was co-polarized with the slot electric field orientation (y). The distance between the EUT and the receiving antenna is 2.3 m, which is smaller than the standard prescription of 3 m due to the environment dimensions and the length constraints of the cables. However, at this distance, the far field condition is fulfilled in the whole analyzed frequency range. Further details of the experimental setup can be found in [18].

The electric field samples were collected using $N_S = 120$ monopoles, irregularly distributed onto the chamber walls. The equivalence surface was chosen as a cube having 30 cm on each side and including the EUT. This choice was made to assure that the equivalence surface always includes the EUT, even in the presence of a small positioning error.

In [17], it has been demonstrated that the distance between two adjacent equivalent sources should be no more than half a wavelength.

In the present case, we chose $2\Delta_x = 2\Delta_y = 2\Delta_z = \lambda/4$. Both in the measurements and in the simulations, the considered frequency was 2 GHz.

Once the scenario is fixed, a quantitative consideration on the advantage of using equivalent currents parallel to the equivalent surface instead of assuming a volumetric placement of magnetic and electric dipoles can be done.

Using a gridding of all the volume included by the equivalent surface, there would be 512 grid points, and by placing three magnetic and three electric currents in each of them, it would need a set of $N_{eq} = 3072$ equivalent sources.

Due to the use of the proposed model, there are only 384 subareas; therefore, $N_{eq} = 1536$. The advantage of the proposed method becomes bigger, increasing the dimensions of the EUT, and consequently of the equivalent surface, in terms of wavelength.

It must be highlighted that the choice of an iterative procedure to find the values of the equivalent sources allows one to have a non-square Z_{ni} matrix. In this way, N_{eq} is chosen to satisfy the constraint on the maximum distance between the equivalent sources, whereas N_S can be limited to a reasonable maximum number for practical reasons (measurement time, number of monopoles and cables, complexity of the switching network).

The reconstruction of the electric field samples is very accurate, and the iterative procedure terminates after reaching the desired accuracy, as shown in Figure 5. For a better readability of the graphics, only the first 20 samples are shown. According to our experience, a value of $err \leq 0.01$ assures a good level of reliability of the algorithm.

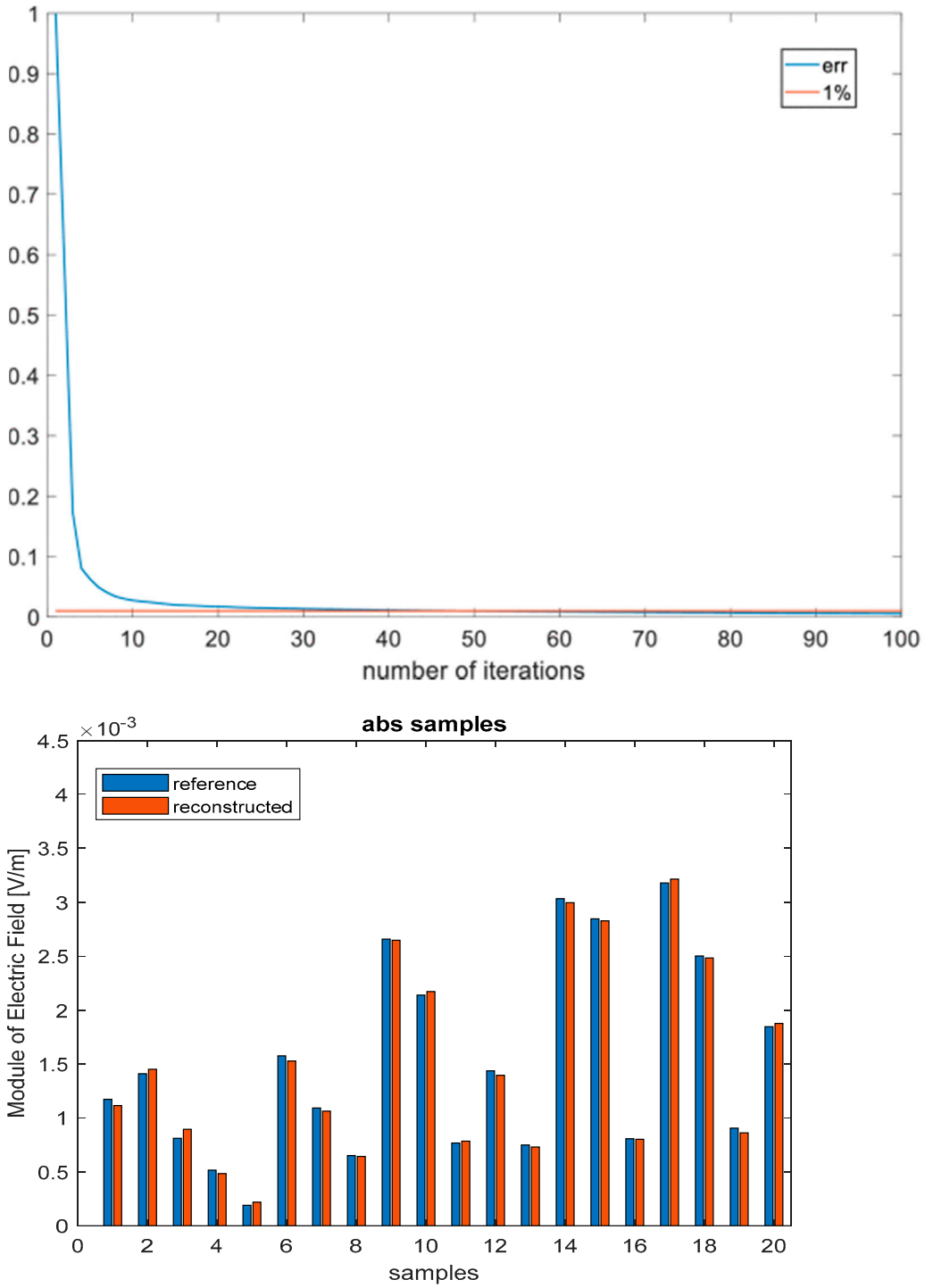

Figure 5. Relative error (err) on the reconstruction of the electric field at samples' position in function of iterations (**up**) and reference and reconstructed electric field samples (**down**).

The same equivalent sources that reconstruct the samples of the electric field collected inside the RC are placed in free space, so that the electric field radiated at a desired distance can be calculated in every direction of the space. Figure 6 reports the emissions calculated at the frequency of 2 GHz. Two planes are considered; according to the reference system of Figure 4, the planes $\phi = 0°$ and $\phi = 90°$ are shown.

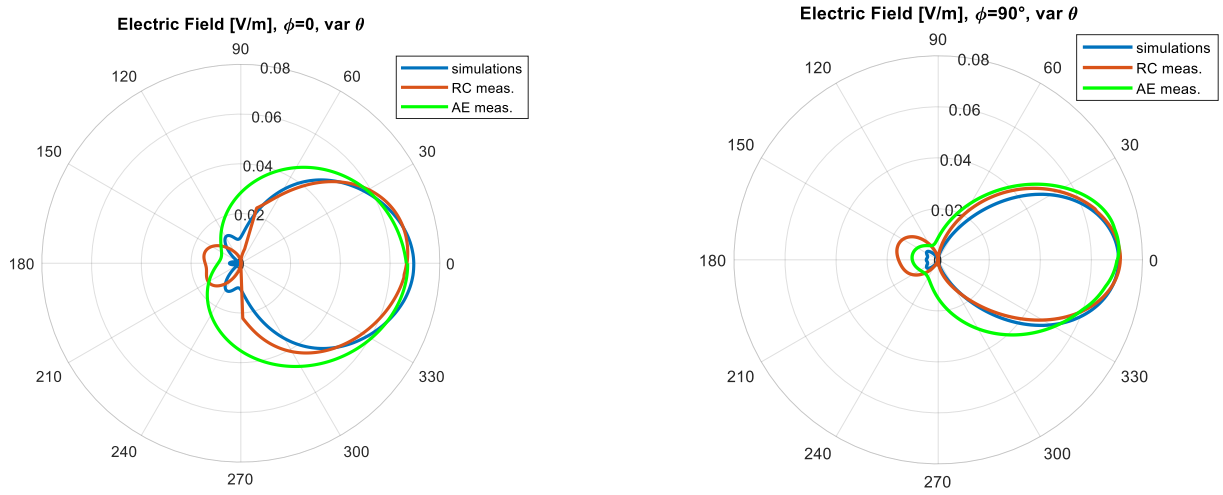

(**a**) (**b**)

Figure 6. Radiated Emissions at the frequency of 2 GHz: (**a**) plane $\phi = 0$ and (**b**) plane $\phi = 90°$ are shown. The comparison reports numerical simulations (blue line), the prediction based on measurements in RC (red line), and measurements in AE (green line).

Figure 7 shows the 3D reconstruction of the emission of the EUT. The good level of agreement between numerical simulations and the prediction from RC measurements, especially in the directions where the radiated field in higher, assures the capability of the method to find the maximum level of electric field radiated over the entirety of the solid angle.

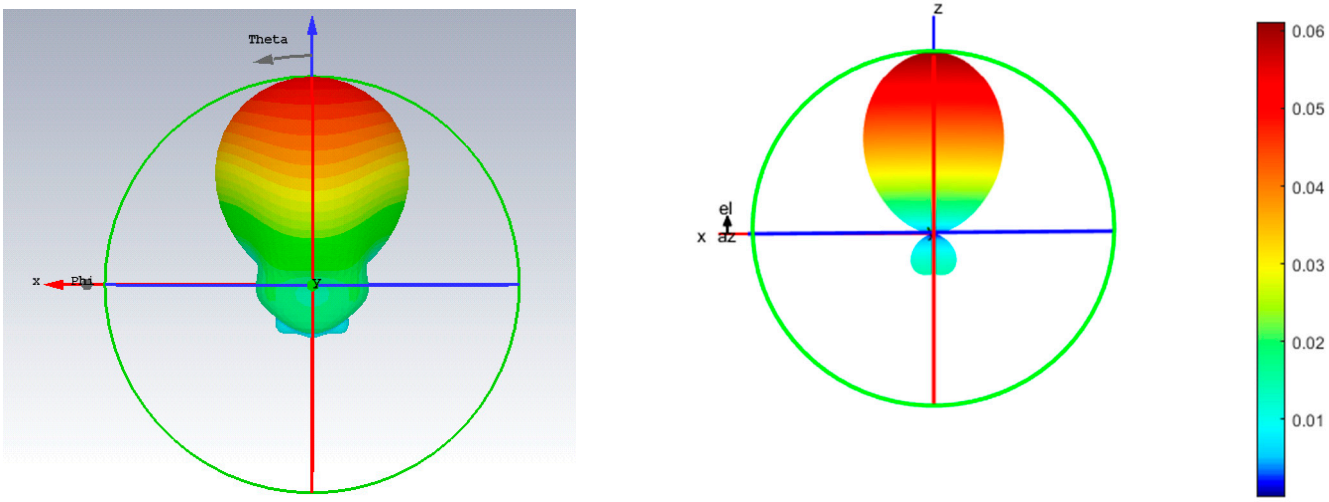

(**a**) (b)

Figure 7. 3D reconstruction of the electric field radiated by the EUT; results of numerical simulations (**a**) and model prediction from measurement in RC environment (**b**) are reported.

This is the final value to be compared with the emission standard limits during a compliance EMC tests. In this sense, the non-perfect reconstruction of the backscattering does not significantly affect the result of an emission test.

4. Discussion

The results reported in the previous section show that the proposed method has a good level of reliability. In particular, the determination of the maximum value of the electric field is the crucial physical quantity in an emission tests because standards fix limits for it.

The capability of reconstruction of the emissions in the entirety of the space assures that the maximum amplitude of the radiated emission is correctly detected.

With respect to the previous formulation of the method [17], there is a reduction of the number of equivalent sources for two reasons. The first one is that they are placed only in the surface surrounding the EUT, while previously they were placed in the entirety of the volume. The second reason is that, due to the application of the equivalence principle, only the tangential electric and magnetic currents are considered. In this way, in each point, only four equivalent sources are considered instead of six.

The computational time is therefore strongly reduced; the simulations presented in this paper stand for about 16 h using a standard workstation (equipped with two CPU Intel Xeon E5640 2.66 GHz, 24 GB of RAM). Applying the precedent version of the method, the computational time was 24 h, using the same workstation.

It must be remarked that the computation of the matrix Z_{ni} is done only once for the considered equivalence surface. This is the most burdensome operation, whereas the rest of the code needs only a few minutes to run. In this direction, the equivalent surface might be extended to the surface of the entire working volume of the RC. This would allow consideration of any EUT, regardless of its geometry; in this way the Z_{ni} computation would represent a type of chamber calibration for the application of the described method.

Finally, using parallel computing, it is possible to calculate Z_{ni} for many frequencies simultaneously.

5. Conclusions

This paper presented an enhanced method to reconstruct the radiated emissions of an EUT in an RC via knowledge of the values of the electric field sampled on the walls. By enforcing the equivalence principle, the number of equivalent sources used to represent the emissions is strongly reduced with respect to other choices. The analytical formulation of the method is based on the use of the modal expansion of the electromagnetic field in a rectangular cavity. The method has been validated using both numerical simulations and experimental measurements performed in an anechoic environment.

Future work will deal with the extension of the proposed method to a scenario where the electric field is sampled using a spectrum analyzer or an EMI receiver, so only the amplitude of the electric field samples is known. Another fundamental aspect that will be investigated is the influence of the loading effect of the chamber, due to the presence of lossy EUTs, on the accuracy of the proposed method.

Author Contributions: Conceptualization, A.D.L., G.C., P.R. and V.M.P.; methodology, G.C.; software, A.D.L.; validation, A.D.L. and V.M.P.; formal analysis, G.C. and P.R.; data curation, A.D.L. and V.M.P.; writing—original draft preparation, A.D.L., G.C., P.R. and V.M.P.; writing—review and editing, A.D.L., G.C., P.R. and V.M.P.; visualization, A.D.L., G.C., P.R. and V.M.P.; supervision V.M.P. All authors who have contributed substantially to the work reported have read and agreed to the published version of the manuscript.

Funding: This research received no external funding.

Institutional Review Board Statement: Not applicable.

Informed Consent Statement: Not applicable.

Conflicts of Interest: The authors declare no conflict of interest.

Appendix A

Appendix A.1. Electric Field Generated by a Sub-Surface Orthogonal to y Axis

Let us consider the rectangular faces of the equivalence surface orthogonal to the y axis and one of its sub-surfaces (S) having dimensions ($2\Delta_x$, $2\Delta_z$), and centered in (x_H,y_H,z_H).

In this case, the equivalent magnetic (M^i_{eq}) and electric (J^i_{eq}) currents are (A1):

$$\begin{cases} \overline{M^i_{eq}} = M^i_{eqx}\hat{x} + M^i_{eqz}\hat{z} \\ \overline{J^i_{eq}} = J^i_{eqx}\hat{x} + J^i_{eqz}\hat{z} \end{cases} \qquad i = 1, \ldots, N^{(y)}_{eq} \tag{A1}$$

where $N^{(y)}_{eq}$ is the total number of sub-areas after the discretization of the considered face.

The electric field radiated by the equivalent currents in a generic point $P(x, y, z)$ is reported in (A2)–(A4).

$$\begin{aligned} \overline{E}_{IRR}(x,y,z) = \; & -\tfrac{1}{j\omega\varepsilon}\tfrac{32}{abc}\sum_{m,n,p}\tfrac{1}{k^2_{m,n,p}}\sin(k_x\Delta_x)\sin(k_yy_H)\sin(k_z\Delta_z)\left[-\tfrac{J^i_{eqx}\sin(k_xx_H)\cos(k_zz_H)}{k_x}\right. \\ & \left.+\tfrac{J^i_{eqz}\cos(k_xx_H)\sin(k_zz_H)}{k_z}\right]\begin{cases} k_x\cos(k_xx)\sin(k_yy)\sin(k_zz)\hat{x} \\ k_y\sin(k_xx)\cos(k_yy)\sin(k_zz)\hat{y} \\ k_z\sin(k_xx)\sin(k_yy)\cos(k_zz)\hat{z} \end{cases}, \end{aligned} \tag{A2}$$

$$\begin{aligned} \overline{E}_{TE}(x,y,z) = \; & \tfrac{32}{abc\delta_m\delta_n}\sum_{m,n,p}\tfrac{1}{k^2_{m,n,p}-\beta^2_{TE}}\sin(k_x\Delta_x)\sin(k_z\Delta_z)\left\{\cos(k_yy_H)\left[\tfrac{M^i_{eqx}\cos(k_xx_H)\sin(k_zz_H)}{k_xk_z}\right.\right. \\ & \left.-\tfrac{M^i_{eqz}\sin(k_xx_H)\cos(k_zz_H)}{k_c^2}\right] \\ & \left.+j\omega\mu\tfrac{k_y}{k_c^2k_x\;k_z}J^i_{eqz}\cos(k_xx_H)\sin(k_yy_H)\sin(k_zz_H)\right\}\begin{cases} -k_y\cos(k_xx)\sin(k_yy)\sin(k_zz)\hat{x} \\ k_x\sin(k_xx)\cos(k_yy)\sin(k_zz)\hat{y} \end{cases} \end{aligned} \tag{A3}$$

$$\begin{aligned} \overline{E}_{TM}(x,y,z) = \; & \tfrac{32}{a\;b\;c\;\delta_p}\sum_{m,n,p}\tfrac{1}{k^2_{m,n,p}-\beta^2_{TM}}\sin(k_x\Delta_x)\sin(k_z\Delta_z)\left\{M^i_{eqz}\tfrac{k_y}{k_x\;k_z}\sin(k_xx_H)\cos(k_yy_H)\cos(k_zz_H)\right. \\ & -j\omega\mu\tfrac{k_c^2}{k^2_{m,n,p}}\sin(k_yy_H)\left[\tfrac{J^i_{eqx}\sin(k_xx_H)\cos(k_zz_H)}{k_x\;k_z}\right. \\ & \left.\left.+\tfrac{J^i_{eqz}\cos(k_xx_H)\sin(k_zz_H)}{k_c^2}\right]\right\}\begin{cases} -\tfrac{k_xk_z}{k_c^2}\cos(k_xx)\sin(k_yy)\sin(k_zz)\hat{x} \\ -\tfrac{k_yk_z}{k_c^2}\sin(k_xx)\cos(k_yy)\sin(k_zz)\hat{y} \\ \sin(k_xx)\sin(k_yy)\cos(k_zz)\hat{z} \end{cases}, \end{aligned} \tag{A4}$$

Where $\beta^2_{TE,TM} = \beta^2[1-1+j)\dfrac{\omega_{n,m,p}}{\omega Q^{TE,TM}_{m,n,p}}$,$\delta_k = \begin{cases} 1, & k \neq 0 \\ 2, & k = 0 \end{cases}$, $k_x = \dfrac{m\pi}{a}, k_y = \dfrac{n\pi}{b}, k_x = \dfrac{p\pi}{c}$.

$\overline{f}_{m,n,p}$ and $\overline{e}^{TE,TM}_{m,n,p}$ are irrotational and TE, TM divergenceless electric eigenvectors respectively, whereas $\overline{h}^{TE,TM}_{m,n,p}$ are the TE, TM divergenceless magnetic eigenvectors.

$k_{m,n,p}$, $Q^{TE,TM}_{m,n,p}$ and $\omega_{n,m,p}$ are the corresponding eigenvalues, quality factors, and resonant angular frequencies, respectively, and $\beta^2 = \omega^2\mu\epsilon$.

Appendix A.2. Electric Field Generated by a Sub-Surface Orthogonal to z Axis

Let us consider the rectangular faces of the equivalence surface orthogonal to the z axis, and one of its sub-surfaces (S) having dimensions ($2\Delta_x, 2\Delta_y$), and centered in (x_H,y_H,z_H).

In this case, the equivalent magnetic and electric currents are (A5):

$$\begin{cases} \overline{M^i_{eq}} = M^i_{eqx}\hat{x} + M^i_{eqy}\hat{y} \\ \overline{J^i_{eq}} = J^i_{eqx}\hat{x} + J^i_{eqy}\hat{y} \end{cases} \qquad i = 1, \ldots, N^{(z)}_{eq} \tag{A5}$$

where $N_{eq}^{(z)}$ is the total number of sub-areas after the discretization of the considered face.

The electric field radiated by the equivalent currents in a generic point $P(x,y,z)$ is reported in (A6)–(A8).

$$\overline{E}_{IRR}(x,y,z) = -\frac{1}{j\omega\varepsilon}\frac{32}{abc}\sum_{m,n,p}\frac{1}{k_{m,n,p}^2}\sin(k_x\Delta_x)\sin(k_y\Delta_y)\sin(k_zz_H)\left[\frac{J_{eqx}^i\sin(k_xx_H)\cos(k_yy_H)}{k_x}\right.$$
$$\left.-\frac{J_{eqy}^i\cos(k_xx_H)\sin(k_yy_H)}{k_z}\right]\begin{cases}k_x\cos(k_xx)\sin(k_yy)\sin(k_zz)\hat{x}\\ k_y\sin(k_xx)\cos(k_yy)\sin(k_zz)\hat{y}\\ k_z\sin(k_xx)\sin(k_yy)\cos(k_zz)\hat{z}\end{cases}, \tag{A6}$$

$$\overline{E}_{TE}(x,y,z) = \frac{32}{abc\delta_m\delta_n}\sum_{m,n,p}\frac{1}{k_{m,n,p}^2-\beta_{TE}^2}\sin(k_x\Delta_x)\sin(k_y\Delta_y)$$
$$\left\{\cos(k_zz_H)\left[\frac{M_{eqx}^i\cos(k_xx_H)\sin(k_yy_H)}{k_x}-\frac{M_{eqy}^i\sin(k_xx_H)\cos(k_yy_H)}{k_y}\right]\right.$$
$$-j\omega\mu\sin(k_zz_H)\left[\frac{J_{eqx}^i\sin(k_xx_H)\cos(k_yy_H)}{k_y}\right. \tag{A7}$$
$$\left.\left.+\frac{J_{eqy}^i\cos(k_xx_H)\sin(k_yy_H)}{k_x}\right]\right\}\begin{cases}-k_y\cos(k_xx)\sin(k_yy)\sin(k_zz)\hat{x}\\ k_x\sin(k_xx)\cos(k_yy)\sin(k_zz)\hat{y}\end{cases}$$

$$\overline{E}_{TM}(x,y,z) = \frac{32}{abc\delta_p}\sum_{m,n,p}\frac{1}{k_{m,n,p}^2-\beta_{TM}^2}\sin(k_x\Delta_x)\sin(k_y\Delta_y)\left\{-\cos(k_zz_H)\left[\frac{M_{eqx}^i\cos(k_xx_H)\sin(k_yy_H)}{k_y}\right.\right.$$
$$\left.+\frac{M_{eqy}^i\sin(k_xx_H)\cos(k_yy_H)}{k_y}\right]$$
$$-j\omega\mu\frac{k_z}{k_{m,n,p}^2}\sin(k_yy_H)\left[-\frac{J_{eqx}^i\sin(k_xx_H)\cos(k_zz_H)}{k_x}\right. \tag{A8}$$
$$\left.\left.+\frac{J_{eqy}^i\cos(k_xx_H)\sin(k_zz_H)}{k_y}\right]\right\}\qquad\begin{cases}-\frac{k_xk_z}{k_c^2}\cos(k_xx)\sin(k_yy)\sin(k_zz)\hat{x}\\ -\frac{k_yk_z}{k_c^2}\sin(k_xx)\cos(k_yy)\sin(k_zz)\hat{y}\\ \sin(k_xx)\sin(k_yy)\cos(k_zz)\hat{z}\end{cases},$$

Where $\beta_{TE,TM}^2 = \beta^2[1-1+j)\frac{\omega_{n,m,p}}{\omega Q_{m,n,p}^{TE,TM}}$, $\delta_k = \begin{cases}1, & k\neq 0\\ 2, & k=0\end{cases}$, $k_x = \frac{m\pi}{a}, k_y = \frac{n\pi}{b}, k_x = \frac{p\pi}{c}$.

$\overline{f}_{m,n,p}$ and $\overline{e}_{m,n,p}^{TE,TM}$ are irrotational and TE and TM are divergenceless electric eigenvectors, respectively, whereas $\overline{h}_{m,n,p}^{TE,TM}$ are the TE and TM divergenceless magnetic eigenvectors.

$k_{m,n,p}$, $Q_{m,n,p}^{TE,TM}$, and $\omega_{n,m,p}$ are the corresponding eigenvalues, quality factors, and resonant angular frequencies, respectively, and $\beta^2 = \omega^2\mu\epsilon$. (*Rev* 2.10).

References

1. Leferink, F.B.; Groot-Boerle, D.J.; Puylaert, B.R. OATS emission data compared with free space emission data. In Proceedings of the International Symposium on Electromagnetic Compatibility, Atlanta, GA, USA, 14–18 August 1995; pp. 333–337.
2. Sreenivasiah, I.; Chang, D.C.; Ma, M.T. Emission of electrically small radiating sources from tests inside a TEM Cell. In Proceedings of the 1979 IEEE International Symposium on Electromagnetic Compatibility, San Diego, CA, USA, 9–11 October 1979.
3. Wilson, P. On correlating TEM cell and OATS emission measurements. *IEEE Trans. Electromagn. Compat.* **1995**, *37*, 1–16. [CrossRef]
4. Wilson, P.F.; Holloway, C.L.; Koepke, G. A review of dipole models for correlating emission measurements made at various EMC test facilities. In Proceedings of the International Symposium on Electromagnetic Compatibility, Silicon Valley, CA, USA, 9–13 August 2004; Volume 3, pp. 898–901.
5. Turnbull, L.; Marvin, A. A treatment of the phase properties of GTEM to open-area test-site correlation techniques. *IEEE Trans. Electromagn. Compat.* **1998**, *40*, 62–69. [CrossRef]
6. Heidemann, M.; Garbe, H. Improvement of GTEM to OATS correlation. In Proceedings of the IEEE International Symposium on Electromagnetic Compatibility. Symposium Record (Cat. No. 00CH37016), Washington, DC, USA, 21–25 August 2000; Volume 2, pp. 909–914.
7. Ngu, X.T.; Nothofer, A.; Thomas, D.W.; Christopoulos, C. A complete model for simulating magnitude and phase of emissions from an EUT placed inside a GTEM Cell. *IEEE Trans. Electromagn. Compat.* **2007**, *49*, 285–293. [CrossRef]

8. Corona, P.; Latmiral, G.; Paolini, E.; Piccioli, L. Use of a reverberating enclosure for measurements of radiated power in the microwave range. *IEEE Trans. Electromagn. Compat.* **1976**, *EMC-18*, 54–59. [CrossRef]
9. Barakos, D.; Serra, R. Performance characterization of the oscillating wall stirrer. In Proceedings of the 2017 International Symposium on Electromagnetic Compatibility—EMC EUROPE, Angers, France, 4–7 September 2017.
10. Leferink, F.; Boudenot, J.-C.; Van Etten, W. Experimental results obtained in the vibrating intrinsic reverberation chamber. In Proceedings of the IEEE Int. Symp. Electromagnetic Compatibility, Washington, DC, USA, 21–25 August 2000; pp. 639–644.
11. Huang, Y.; Edwards, D.J. A novel reverberating chamber: Source-stirred chamber. In Proceedings of the IEEE 8th International Conference on Electromagnetic Compatibility, Edinburgh, UK, 21–24 September 1992; pp. 120–124.
12. De Leo, A.; Primiani, V.M.; Russo, P.; Cerri, G. Low-frequency theoretical analysis of a source-stirred reverberation chamber. *IEEE Trans. Electromagn. Compat.* **2016**, *59*, 315–324. [CrossRef]
13. De Leo, A.; Cerri, G.; Russo, P.; Primiani, V.M. Experimental validation of an analytical model for the design of source-stirred chambers. *IEEE Trans. Electromagn. Compat.* **2017**, *60*, 540–543. [CrossRef]
14. De Leo, A.; Primiani, V.M.; Russo, P.; Cerri, G. Numerical analysis of a reverberation chamber: Comparison between mechanical and source stirring techniques. In Proceedings of the 2017 International Symposium on Electromagnetic Compatibility—EMC Europe, Angers, France, 4–7 September 2017.
15. De Leo, A.; Cerri, G.; Russo, P.; Primiani, V.M. Experimental comparison between source stirring and mechanical stirring in a reverberation chamber by analyzing the antenna transmission coefficient. In Proceedings of the 2018 International Symposium on Electromagnetic Compatibility (EMC Europe), Amsterdam, The Netherlands, 27–30 August 2018; pp. 677–682.
16. International Electrotechnical Commission—IEC. *Reverberation Chamber Test Methods—Std. 61 000-4-21*; IEC: Geneva, Switzerland, 2011.
17. De Leo, A.; Cerri, G.; Russo, P.; Primiani, V.M. A general method for radiated emission prediction in a multiple monopole source stirred reverberation chamber. *IET Sci. Meas. Technol.* **2021**, *15*, 588–596. [CrossRef]
18. Van Bladel, J.G. *Electromagnetic Fields*; IEEE Press Series on Electromagnetic Wave Theory; Wiley: Hoboken, NJ, USA, 2007; pp. 509–562.